*JBIS, Vol. 60, pp.28-39, 2007*

# DETECTING PATTERNS OF A TECHNOLOGICAL INTELLIGENCE IN REMOTELY SENSED IMAGERY

**MARK J. CARLOTTO**
*8 Milne Way, Gloucester, MA 01930, USA.*
Email: markcarlotto@adelphia.net

A statistical classification approach for detecting artificial patterns in satellite imagery such as those produced by a technological intelligence, and its application to the search for non-natural features of possible extraterrestrial origin on planetary surfaces is presented. Statistics of natural terrestrial backgrounds (fractal textures, drainage patterns, tectonic features, etc.) and artificial features (e.g., roads, cities, vehicles, archaeological ruins) are computed over a set of terrestrial training images. Images are represented by measurements of their fractal dimension, fractal model fit, anisotropy, and rectilinearity. The likelihood ratio (conditional probability of a measurement given it is artificial divided by the conditional probability of a measurement given it is natural) is used as an index for assessing the artificiality of an unknown image relative to the training set. A classification accuracy of 85% is achieved over a training set of terrestrial images. The statistics of the training set are then extended to assess a number of enigmatic lunar and planetary features. Results suggest that certain areas on our moon and on Mars appear to be artificial by comparison with terrestrial features.

**Keywords:** Search for Extraterrestrial Intelligence (SETI), archaeological remote sensing, planetary imaging, fractals, comparative analysis

## 1. INTRODUCTION

Human activities have transformed our planet. Forests have been cleared for agriculture, human settlements have become vast urban sprawls that can be seen from space. Patterns of intelligence are everywhere. Even places that had been abandoned and were once forgotten have been rediscovered by archaeologists trained to recognize the subtle patterns of prior human habitation in aerial imagery.

Originally, the goal in the search for extraterrestrial intelligence (SETI) was to detect the existence of extraterrestrial life by their radio frequency (microwave) emissions [1]. More recently its scope has expanded to include the search for extraterrestrial intelligence at optical frequencies [2], and the search for extraterrestrial artifacts (SETA) in our solar system [3, 4]. This paper is concerned with the problem of detecting artificial patterns in satellite imagery produced by a technological intelligence, and its application to the search for non-natural objects and features of possible extraterrestrial origin on planetary surfaces (pSETI), which is a subset of SETA.

Human observers have an innate ability to differentiate between natural and artificial objects and patterns – whether they are a group of military vehicles deployed in a complex battlefield scene or a modulated signal in radio noise, but may be predisposed to see patterns of intelligence where there are none (e.g., faces in clouds). There are many examples of this in the history of science from Gruithuisen's walled city on the moon to the canals on Mars. Although machine algorithms are free from such bias, attempts at developing algorithms that operate at levels comparable to human performance have not been entirely successful.

This paper was presented at the British Interplanetary Society "Archaeology for Space" Symposium on 10th May 2006.

Carl Sagan [5] argued that deviations from thermodynamic equilibrium are a necessary (but not sufficient) condition of intelligent activity. He cited significant deviations from the blackbody radiation curve of Earth in the radio frequency portion of the electromagnetic spectrum as evidence of terrestrial intelligence, and went on to show that passive (electro-optical) imaging of Earth at resolutions (spatial scales) smaller than about 1 km reveals evidence of mechanical disequilibrium (e.g., rectilinear patterns of agriculture, road networks, etc.).

Landscapes can be thought of as thermodynamic systems (where elevation is equivalent to temperature and mass to heat) that seek close-to-equilibrium states where the rate of entropy production is minimized [6]. Emergent properties of landscapes have been shown to have fractal (or multifractal) characteristics [7, 8]. Analogous to the way intelligent activity on a planetary scale reveals itself as deviations from blackbody radiation in the radio frequency spectrum on Earth, Stein [9] developed a method for finding manmade features in images by detecting deviations from a fractal model of the background. Carlotto and Stein [10] applied the same technique to assess the artificiality of certain Martian landforms. Arkhipov [11] combined fractal analysis with other techniques to detect lunar anomalies.

Directionally-correlated structures are common in images of artificial features – from the rectangularity and symmetry of isolated objects like vehicles and buildings, to straight lines and rectilinear patterns in extended features like today's cities. Even in archaeological ruins where fine structure is obscured by deposition and erosion, evidence of extended linear and rectilinear structures are often visible [12]. On the other hand, correlated spatial structures appear quite frequently in nature.

Examples include geological faults, certain patterns of erosion, as well as long cast shadows from tall objects such as trees. Thus while directionally-correlated structure is often present in images containing artificial features (a necessary condition), it is not sufficient in itself in determining artificiality.

This paper proposes a comparative statistical pattern recognition approach to the problem of detecting patterns of a technical intelligence in remotely sensed imagery. Section 2 describes methods for distinguishing between images of natural and artificial features in terms of the fractal dimension (the roughness of the image intensity surface), fractal model fit (how well an image is modeled as a fractal), anisotropy (the directional correlation structure), and rectilinearity (presence of correlated structures at right angles). These methods are applied to a small database (Section 3) containing images of natural terrestrial backgrounds, manmade objects and features (including images of archaeological sites in various stages of decay), and images of interesting planetary features. Using the terrestrial data, a maximum likelihood classifier is developed and applied to the planetary data set. Analysis of results (Section 4) reveals that certain features on our moon and on Mars appear to be artificial by comparison with terrestrial features. Limitations of the pattern recognition technique resulting from the confusion of manmade objects that look natural (highly eroded archaeology), and natural objects that look artificial (geological features like the San Andreas fault) are discussed. Future directions are outlined in Section 5.

## 2. MEASURING ARTIFICIALITY

Fractals [13] are objects that are self-similar over a range of scales. Examples of fractals include clouds, snow flakes, mountains, and drainage patterns. Fractal object detection assumes the natural background in an image can be modeled as a fractal, whose measurements follow power laws of the form

$$Y = Y_0 X^b \tag{1}$$

where $Y$ is the value of a measurement, $X$ is the scale of the measurement, $b$ is related to the fractal dimension, $Y_0$ and is a constant. Measurement techniques include variograms, which measure the variance as a function of distance, morphological filters, which estimate the surface area of the image intensity surface as a function of scale (resolution), and the power spectral density, which measures power vs. frequency.

Stein [10] used a set of morphological filters to measure the surface area of the image intensity over a range of scales, from which he estimated the fractal dimension and fractal model-fit error that were used as features for detecting manmade objects. Here we use the power spectral density (PSD) as it leads to other useful measures for assessing artificiality. For a 1-D signal with PSD $S(k)$ the power law is

$$S(k) \propto 1/k^{\beta} \tag{2}$$

For $1<\beta<3$ the fractal dimension $D = 2 + (3 - \beta)/2$ is $3>D>2$. Now consider a 2-D image with PSD $S(m,n)$, and radial distribution

$$S(k) = \sum_{\theta=0}^{2\pi} S(m = k\cos\theta, n = k\sin\theta) \tag{3}$$

For spatially isotropic 2-D PSDs the 1-D radial distribution (3) is the same as the 1-D PSD along a line in any direction in the image. Voss [14] shows that the 2-D power law is

$$S(m,n) \propto 1/(m^2 + n^2)^{(\beta+1)/2} = 1/k^{\beta+1} \tag{4}$$

Linear regression of measurements of $\log S(k)$ vs. $\log k$ can be used to estimate the spectral exponent, $b$ from which the fractal dimension is obtained. The model fit (normalized correlation) tests the validity of the fractal assumption

$$M = \sigma_{kS}^2 \Big/ \sqrt{\sigma_k^2 \sigma_S^2} \tag{5}$$

where the statistics

$$\sigma_k^2 = \left\langle \log k^2 \right\rangle_K - \left\langle \log k \right\rangle_K^2 ,$$
$$\sigma_S^2 = \left\langle \log S(k)^2 \right\rangle_K - \left\langle \log S(k) \right\rangle_K^2 ,$$
$$\sigma_{kS}^2 = \left\langle \log k \log S(k) \right\rangle_K - \left\langle \log k \right\rangle_K \left\langle \log S(k) \right\rangle_K$$

are computed over spatial frequency; i.e.

$$\left\langle \ \right\rangle_K = \frac{1}{K} \sum_{k=0}^{K-1} .$$

Fractals have model fit values close to one.

Carlotto [12] compared geospatial anisotropies (directions of greater correlation) in variograms of images over the Cydonia region of Mars to that of terrestrial archaeological sites. The 2-D PSD is the inverse discrete Fourier transform of the autocorrelation function, which is related to the variogram. Large values of the variogram in a given direction indicates the presence of correlated structure in the image in the same direction. Correlated structures also manifest themselves in the 2-D PSD, which is easier to compute than the variogram. To this end we define the angular distribution

$$F(\theta) = \sum_{k=0}^{K-1} S(m = k\cos\theta, n = k\sin\theta) \tag{6}$$

Let $\mu_A$ and $\sigma_A$ be the mean and standard deviation of $F(\theta)$ over the angular range 0 to $2\pi$; i.e., $\mu_A = \left\langle F(\theta) \right\rangle_{2\pi}$ and

$$\sigma_A = \sqrt{\left\langle F^2(\theta) \right\rangle_{2\pi} - \mu_A^2}$$

We define the anisotropy of the 2-D PSD to be

$$A = \frac{\max_{2\pi} F(\theta) - \mu_A}{\sigma_A} \tag{7}$$

Images that have directional structure have larger values of $A$ than those that do not.

Another useful property is the rectilinearity, which measures the presence of directional structures 90° apart. If the direction with the most power is

$$\theta_A = \arg\max_{2\pi} F(\theta) \tag{8}$$

define

$$\Omega : \theta_A + \frac{\pi}{2} - \delta \le \theta \le \theta_A + \frac{\pi}{2} + \delta \qquad (9)$$

to be the angular range to search for rectilinear features. For perfectly rectangular features $\delta = 0$. Providing a tolerance ($\delta > 0$) is useful in cases when the images are oblique and rectangular features appear as parallelograms (due to foreshortening) with right angles in range becoming obtuse and right angles in cross-range acute.

Let $\mu_R = \langle F(\theta) \rangle_\Omega$ and

$$\sigma_R = \sqrt{\langle F^2(\theta) \rangle_\Omega - \mu_R^2}$$

be the mean and variance within the interval (9), and

$$\theta_R = \arg\max_\Omega F(\theta)$$

be the angle of the peak. We define the rectilinearity to be the ratio

$$R = \frac{F(\theta_R) - \mu_R}{\sigma_R} \Big/ \frac{F(\theta_A) - \mu_R}{\sigma_R} = \frac{F(\theta_R) - \mu_R}{F(\theta_A) - \mu_R} \qquad (10)$$

whose maximum value is one when the second peak is as large as the first.

## 3. TEST DATA

A small but diverse set of images have been compiled for analysis. They are divided into three classes: terrestrial images of natural backgrounds (Fig. 1), terrestrial images of artificial objects and patterns (Fig. 2), and extraterrestrial (planetary) images of some "interesting" features (Fig. 3). The images in Fig. 1 are as follows:

a) Badlands in western South Dakota (US). The Badlands contain a variety of formations resulting from severe erosion of the clay-rich soil by wind and rain.

b) Mountains near the Caspian Sea. The image is a computer graphics rendering (shaded rendition) of the elevation map in h).

c) Forested area in winter on Cape Ann Massachusetts (US), in a region known as Dogtown. Cast shadows from pine trees produce a strong directional component in the image.

d) Image of a drainage pattern in Yemen. (Similar drainage patterns can be found on Mars.)

e) Aerial image containing trees and bushes. Some vehicle tracks are also evident on the ground.

f) Computer graphics rendering of the synthetic fractal surface in i).

g) Section of the San Andreas fault in California (US).

h) Elevation map of mountains near the Caspian Sea.

i) Synthetic fractal surface (D=2.5).

Although these images are far from being either complete or statistically representative of all of the different kinds of natural terrestrial backgrounds, they do provide a sampling of the range of background types one may encounter.

The images in Fig. 2 are of artificial objects and structures on the Earth's surface. The majority are of archaeological sites having different (subjective) degrees of erosion. The images are as follow:

a) La Centinela (Peru). These structures were built several hundred years before the Inca occupation in 1450.

b) Chotuna (Peru). Adobe pyramid and surrounding irrigation canals were built around 600 AD.

c) Urban area in the US.

d) Abandoned road on Cape Ann Massachusetts. The road, which was built by colonial settlers, has not been used since the early 1800's.

e) Nasca lines, Peru. The origin and purpose of this vast network of lines and geoglyphs is unknown.

f) Structure within unexplored ruins in Viru Valley (Peru).

g) Less distinct section of ruins in Viru Valley.

h) Sipan (Peru). Eroded pyramids dated to around 300 AD.

i) Pentagon building (US).

j) Military tank.

k) Military truck.

Figure 3 is a sampling of some interesting planetary features that have been encountered over the last 40 years since Lunar Orbiter:

a) Ice flows on Jupiter's moon Europa (Galileo).

b) "Face on Mars" (Mars Global Surveyor).

c) Rim around Saturn's moon Iapetus. Image from a section of an image map constructed from a number of images taken by the Cassini spacecraft.

d) Portion of Arabia Terra on Mars containing a number of tracks lefts by dust devils (MGS).

e) Section of Mars Digital Image Map over Cydonia region of Mars. Derived from Viking Orbiter imagery.

f) Mesas on the Elysium Plains of Mars (MGS).

g) Lunar Orbiter image of rectangular depressions near the crater Ariadaeus B on the moon.

h) Lunar Orbiter image of a rectilinear formation next to the crater Ukert.

i) Clementine image of rectilinear "scrapings" on the far side of the moon.

j) Unusual formations ("spiders") around Chasma Australe at the south pole of Mars [16].

k) THEMIS image of rectilinear texture in Cydonia, Mars.

l) Rectangular arrangements of mesas in Cydonia (Viking Orbiter).

Table 1 lists the computed values of the fractal dimension, fractal model fit, anisotropy, and rectilinearity for all 32 images in Figs. 1-3. Image sizes ranged from 32 x 32 to 512 x 512 pixels, with resolutions from less than a meter to more than a kilometer per pixel. Note the shaded rendering (fr) of the fractal surface (zfr) has a higher fractal dimension, lower model fit, and higher anisotropy than the original surface. The increase in anisotropy is caused by the presence of correlated structures in the image perpendicular to the illuminant direction. Interestingly the situation is reversed in the shaded render-

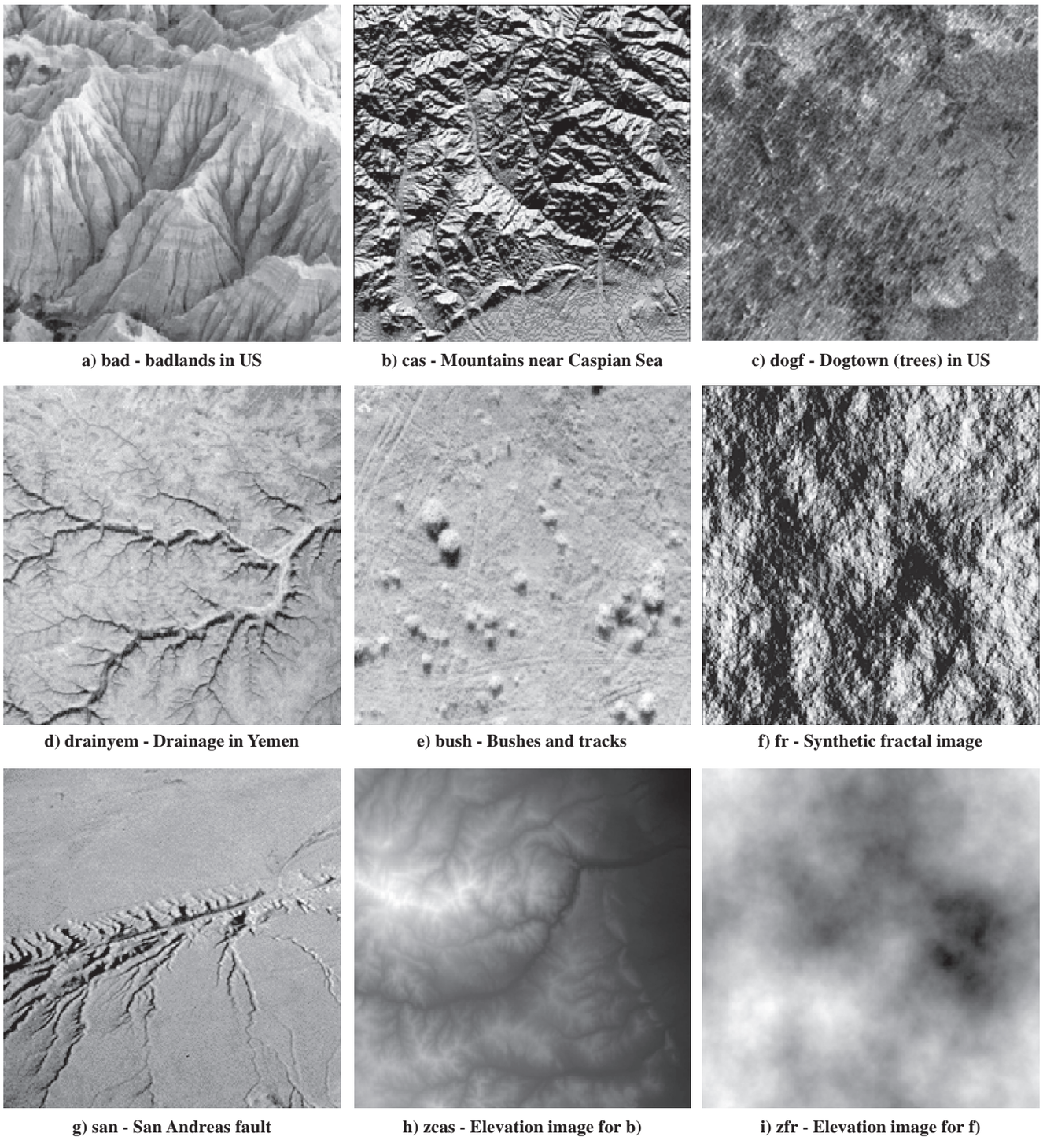

**a) bad - badlands in US** **b) cas - Mountains near Caspian Sea** **c) dogf - Dogtown (trees) in US**

**d) drainyem - Drainage in Yemen** **e) bush - Bushes and tracks** **f) fr - Synthetic fractal image**

**g) san - San Andreas fault** **h) zcas - Elevation image for b)** **i) zfr - Elevation image for f)**

**Fig. 1 Aerial images of natural terrestrial (and synthetic fractal) backgrounds.**

ing (cas) of the mountain range (zcas), where the illuminant direction is roughly perpendicular to the tectonics and has the effect of reducing the anisotropy.

## 4. CLASSIFICATION RESULTS

First we examined how individual measures correlate with image class (top row in Table 2). The fractal dimension has the lowest degree of correlation, providing practically no separation between the natural and artificial images. Next comes the anisotropy which has a low value due to the presence of highly correlated structures in natural backgrounds (e.g., San Andreas fault), and less correlated structures in the older archaeological sites. The fractal model fit was slightly higher but is positively correlated with class; i.e., large values of model fit correspond to artificial features. This is a surprise as the model fit was originally designed to detect non-fractal (non-natural) features (and thus should be negatively correlated). In Stein's original approach he measured the fractal dimension and model fit

a) cent - La Centinela, Peru

b) ch - Chotuna, Peru

c) City (US)

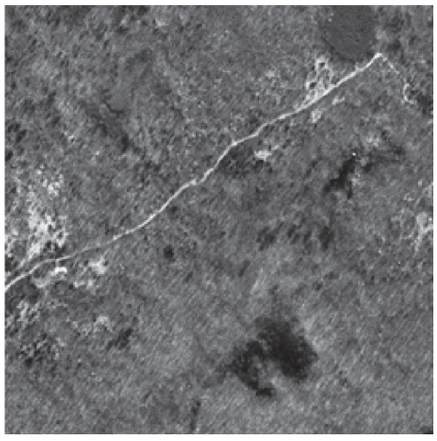

d) dogr - Dogtown (road) in US

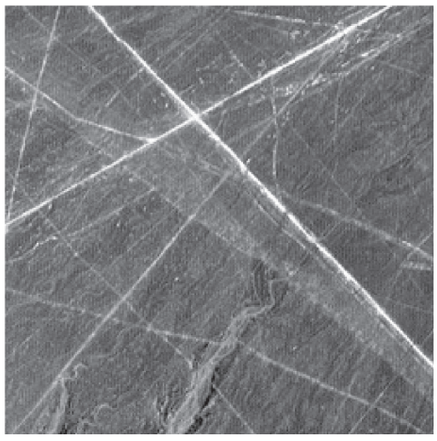

e) nasca - Nasca lines, Peru

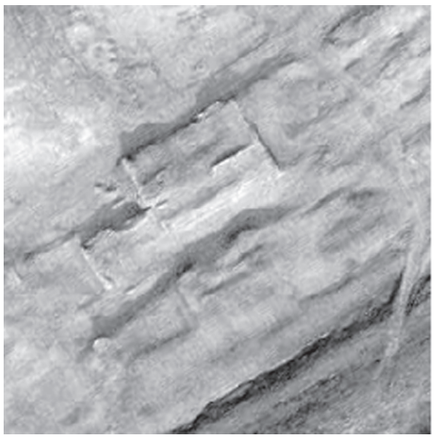

f) vira - Ruins in Viru Valley, Peru

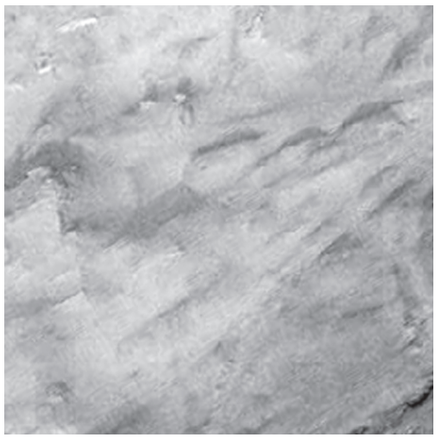

g) virb - More ruins in Viru Valley

h) sip - Pyramid in Sipan, Peru

i) penta - Pentagon in US

j) tank

k) truck

**Fig. 2 Aerial images of manmade objects and features. (Images of Peru courtesy Marilyn Bridges [15].)**

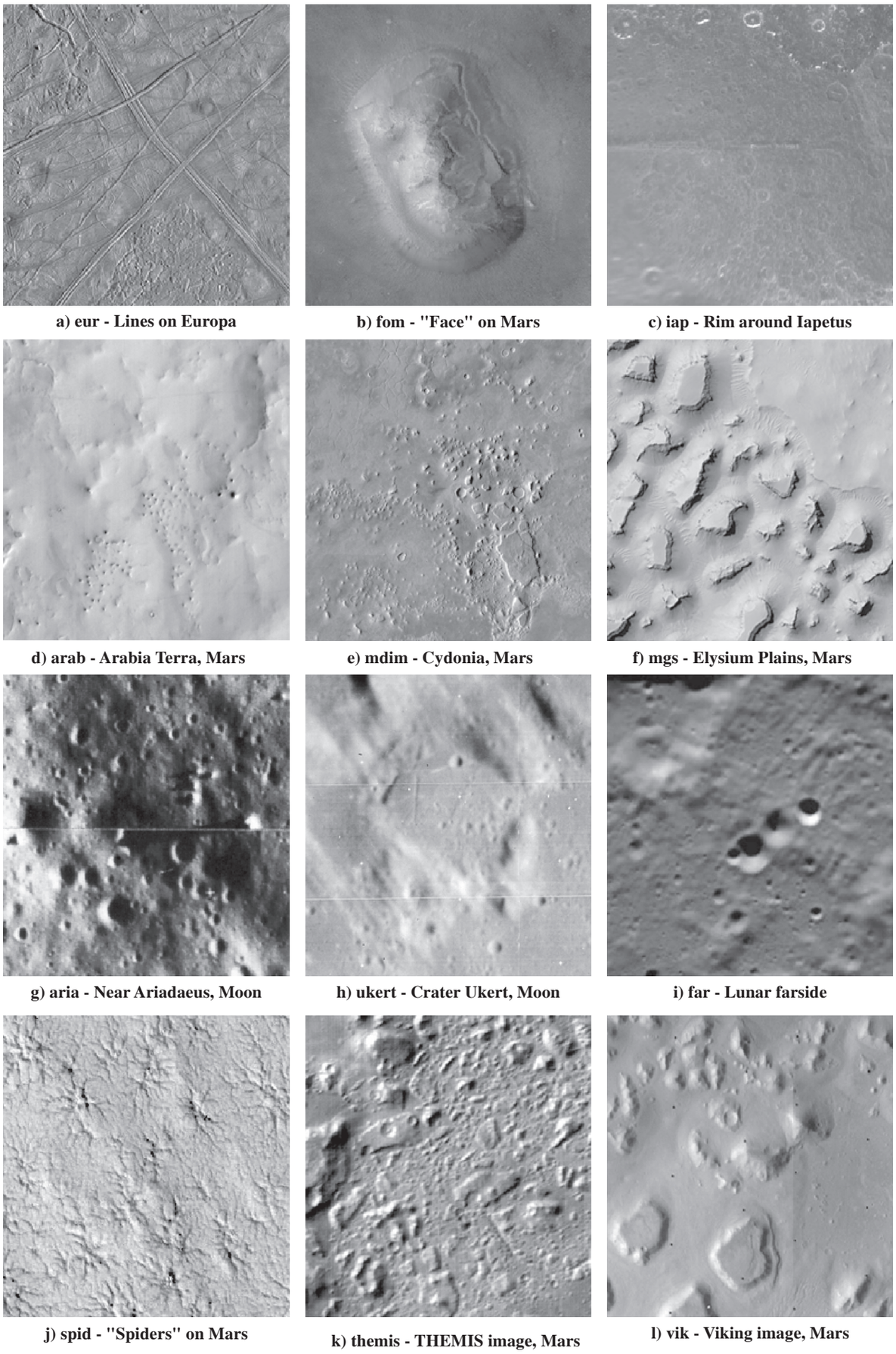

**a) eur - Lines on Europa**
**b) fom - "Face" on Mars**
**c) iap - Rim around Iapetus**
**d) arab - Arabia Terra, Mars**
**e) mdim - Cydonia, Mars**
**f) mgs - Elysium Plains, Mars**
**g) aria - Near Ariadaeus, Moon**
**h) ukert - Crater Ukert, Moon**
**i) far - Lunar farside**
**j) spid - "Spiders" on Mars**
**k) themis - THEMIS image, Mars**
**l) vik - Viking image, Mars**

**Fig. 3 Satellite images of "interesting" features from Europa, Mars, Iapetus, and the Moon (NASA).**

**TABLE 1:** *Image Descriptions and Measurements. Image Sizes in Pixels. Classes are Natural (-1), Artificial (1), and Unknown (0).*

| Image | Size | Description | Class | Fractal Dimension | Fractal Model Fit | Anisotropy | Rectilinearity |
|---|---|---|---|---|---|---|---|
| city | 256 | Section of urban area (US) | 1 | 2.894106 | 0.984046 | 2.982445 | 0.941044 |
| nasca | 256 | Nasca lines (Peru) | 1 | 2.887811 | 0.977394 | 6.013621 | 0.303069 |
| apc | 32 | APC (truck) | 1 | 1.807446 | 0.991947 | 2.853991 | 0.633921 |
| penta | 512 | Pentagon (US) | 1 | 2.77867 | 0.988861 | 3.979506 | 0.877651 |
| tank | 64 | Military tank | 1 | 2.235304 | 0.991981 | 2.568841 | 0.311998 |
| dogr | 512 | Abandoned road in Dogtown, MA (US) | 1 | 2.780654 | 0.973971 | 3.571972 | 0.359881 |
| cent | 512 | Ruins in La Centinela, (Peru) | 1 | 2.721839 | 0.990773 | 1.997346 | 0.471783 |
| ch | 512 | Eroded pyramid in Chotuna (Peru) | 1 | 2.850466 | 0.997328 | 2.260062 | 0.621099 |
| vira | 256 | More distinct ruins in Viru Valley (Peru) | 1 | 2.514642 | 0.991413 | 2.488078 | -0.027554 |
| virb | 256 | Less distinct ruins in Viru Valley (Peru) | 1 | 2.474378 | 0.98537 | 1.890924 | 0.861864 |
| sip | 512 | Highly eroded pyramid in Sipan (Peru) | 1 | 2.735487 | 0.982141 | 1.837547 | 0.753127 |
| san | 256 | San Andreas fault (US) | -1 | 2.910171 | 0.944952 | 4.003116 | 0.23552 |
| zcas | 512 | Mountain DEM (Europe) | -1 | 2.157554 | 0.994076 | 2.294654 | 0.197835 |
| bad | 512 | Badlands (US) | -1 | 2.337011 | 0.98841 | 1.99849 | 0.160731 |
| bush | 256 | Bushes | -1 | 2.68692 | 0.986457 | 2.257377 | 0.187683 |
| fr | 512 | Shaded rendition of synthetic fractal DEM | -1 | 2.883349 | 0.986841 | 2.101432 | -0.810003 |
| drainyem | 256 | Drainage pattern (Yemen) | -1 | 2.720381 | 0.976804 | 2.201048 | 0.049151 |
| cas | 512 | Shaded rendition of mountain DEM (Europe) | -1 | 2.829427 | 0.984636 | 1.877927 | -0.978623 |
| dogf | 512 | Forested area in Dogtown, MA (US) | -1 | 2.64402 | 0.959653 | 2.625042 | 0.427277 |
| zfr | 512 | Synthetic fractal DEM | -1 | 2.296282 | 0.990175 | 1.783851 | 0.497391 |
| iap | 256 | Rim around Iapetus | 0 | 2.862102 | 0.943964 | 3.003908 | 0.707153 |
| ukert | 256 | Rectangular feature near Ukert crater (Moon) | 0 | 2.48217 | 0.9949 | 2.731123 | 0.702401 |
| vik | 512 | Rectilinear arrangement of mesas in Cydonia (Mars) | 0 | 2.550116 | 0.989696 | 3.374994 | 0.077931 |
| arab | 512 | Portion of Arabia Terra (Mars) | 0 | 2.663123 | 0.982713 | 2.892422 | 0.554262 |
| aria | 256 | Rectangular depressions near Ariadaeus B (Moon) | 0 | 2.377679 | 0.981655 | 1.908456 | 0.47908 |
| eur | 512 | Ice patterns (Europa) | 0 | 3.181974 | 0.926466 | 3.43557 | 0.611663 |
| spid | 256 | Spider patterns near Chasma Australe (Mars) | 0 | 2.864983 | 0.963355 | 1.852838 | 0.560556 |
| mgs | 512 | Mesas on Elysium plains (Mars) | 0 | 2.359254 | 0.975722 | 1.392996 | -1.280682 |
| fom | 256 | “Face” in Cydonia region (Mars) | 0 | 2.798049 | 0.989013 | 2.067401 | 0.153125 |
| far | 256 | Patterned ground on far side (Moon) | 0 | 2.76403 | 0.958454 | 2.258627 | -0.46086 |
| mdim | 512 | Overview image map of Cydonia region (Mars) | 0 | 2.76403 | 0.958454 | 2.258627 | -0.46086 |
| themis | 256 | Rectilinear texture in Cydonia (Mars) | 0 | 2.517063 | 0.939568 | 1.773875 | 0.718761 |

**TABLE 2:** *Normalized Correlations for Terrestrial Images. Rectilinearity Measurement is Most Correlated with Natural/Artificial Class, While Fractal Dimension is Least Correlated.*

| | Class | Fractal Dimension | Fractal Model Fit | Anisotropy | Rectilinearity |
|---|---|---|---|---|---|
| **Class** | - | 0.000187665 | 0.318513685 | 0.296424467 | 0.576546231 |
| **Fractal Dimension** | 0.000187665 | - | -0.402182284 | 0.295043422 | -0.171770136 |
| **Fractal Model Fit** | 0.318513685 | -0.402182284 | - | - 0.412377799 | 0.038764788 |
| **Anisotropy** | 0.296424467 | 0.295043422 | -0.412377799 | - | 0.180198714 |
| **Rectilinearity** | 0.576546231 | -0.171770136 | 0.038764788 | 0.180198714 | - |

using morphological techniques over a limited range of scales within a sliding window in the image. The range of scales were those over which manmade objects (vehicles) are different from trees, bushes, and other types of natural background clutter. Here we use a different technique (spectral estimation) that is applied to the entire image. Over larger areas image backgrounds can be multifractal or periodic which produce higher model fit errors than manmade objects and features. The rectilinearity had the highest correlation due to the lack of rectilinear features in the natural backgrounds we studied. The high degree of correlation is also consistent with earlier findings [12] which indicate that edges and other extended features persist even in highly eroded archaeological sites.

Let us define $\mathbf{z}$ to be the measurement vector consisting of the fractal dimension, fractal model fit, anisotropy, and rectilinearity. Assume the measurements are jointly Gaussian random variables, i.e.,

$$p(\mathbf{z}) = \frac{1}{(2\pi)^{N/2}|\mathbf{C}|^{1/2}} \exp -\tfrac{1}{2}(\mathbf{z}-\mathbf{m})^T \mathbf{C}^{-1}(\mathbf{z}-\mathbf{m}) = N(\mathbf{m},\mathbf{C}) \tag{11}$$

where $\mathbf{m} = E[\mathbf{z}]$ is the mean vector,

$$\mathbf{C} = E\left[(\mathbf{z}-\mathbf{m})(\mathbf{z}-\mathbf{m})^T\right]$$

is the covariance matrix, $|\mathbf{C}|$ is the determinant of $\mathbf{C}$, and $E$ is the expectation operator. Here $N = 4$. If $\omega_0$ is the set of images of natural backgrounds in Fig. 1, and $\omega_1$ is the set of images of artificial objects and features in Fig. 2, the class-conditional means and variances are:

$$\begin{aligned} &\mathbf{m}_0 = E[\mathbf{z}|\mathbf{z}\in\omega_0] \quad \mathbf{m}_1 = E[\mathbf{z}|\mathbf{z}\in\omega_1] \\ &\mathbf{C}_0 = E\left[(\mathbf{z}-\mathbf{m}_0)(\mathbf{z}-\mathbf{m}_0)^T|\mathbf{z}\in\omega_0\right] \\ &\mathbf{C}_1 = E\left[(\mathbf{z}-\mathbf{m}_1)(\mathbf{z}-\mathbf{m}_1)^T|\mathbf{z}\in\omega_1\right] \end{aligned} \tag{12}$$

The conditional densities are thus $p(\mathbf{z}|\omega_0) = N(\mathbf{m}_0,\mathbf{C}_0)$ and $p(\mathbf{z}|\omega_1) = N(\mathbf{m}_1,\mathbf{C}_1)$.

The likelihood ratio $p(\mathbf{z}|\omega_1)/p(\mathbf{z}|\omega_0)$ is greater than one for images that are more likely to contain artificial features. Although some of the measurements do have a certain degree of correlation (e.g., fractal dimension and fractal model fit), we assume the measurements are uncorrelated. This allows us to express the logarithm of the likelihood ratio as a sum of individual log likelihoods:

$$\begin{aligned} \eta &= \ln\left[p(\mathbf{z}|\omega_1)/p(\mathbf{z}|\omega_0)\right] \\ &= \ln\frac{p(D|\omega_1)}{p(D|\omega_0)} + \ln\frac{p(M|\omega_1)}{p(M|\omega_0)} + \ln\frac{p(A|\omega_1)}{p(A|\omega_0)} + \ln\frac{p(R|\omega_1)}{p(R|\omega_0)} \end{aligned} \tag{13}$$

Table 3 lists the individual and summed log likelihoods based on the statistics in Table 4. Figure 4 plots the summed log likelihoods of all of the images. Over the "training set"; i.e., the set of terrestrial images, 17 out of 20 images are correctly classified (i.e., $\eta > 0$ if the images are artificial) using all four measurements. Other combinations were 16/20 using only rectilinearity, 11/20 using only anisotropy, 15/20 using anisotropy and rectilinearity, and 12/20 using only fractal model fit.

Figure 5 sorts and plots the results by class. Five of the 12 extraterrestrial images – ukert, arab, far, aria, and vik – had positive log likelihood values, which indicates that they appear more artificial than natural based on the training set. In order to better understand the results we measure the similarity between the terrestrial images in Figs. 1 and 2, and the planetary images in Fig. 3. The Mahalanobis distance between measurement vectors

$$d(\mathbf{z}_i,\mathbf{z}_j) = (\mathbf{z}_i-\mathbf{z}_j)^T \mathbf{C}^{-1}(\mathbf{z}_i-\mathbf{z}_j) \tag{14}$$

is used to rank-order and sort the terrestrial images most like each planetary image (Table 5). Each column contains a rank-ordering of terrestrial images in terms of their similarity to the planetary image listed at the top. This provides a set of terrestrial analogs for comparative analysis. For example, the rim around Iapetus (iap) is similar to the forested background over Dogtown (dogf), the San Andreas fault (san), and the abandoned road (dogr). It is least similar to a truck (apc). The feature near Ukert is similar to the ruins in Viru (vira), the tank, and the ruins in La Centinela (cent). It is least similar to the Nasca lines. In fact, the Nasca lines are least similar to all of the extraterrestrial features overall. The natural background containing trees, bushes, and vehicle tracks (bush) is the most frequent terrestrial analog. The "Face" on Mars (fom) is similar to the bush image followed by the ruins in La Centinela (cent), and the drainage pattern in Yemen (drainyem). Perhaps the latter is due to the presence of erosional features on the "Face". The overall similarity of terrestrial features to the set of planetary features is listed in Table 6. This table was obtained by computing the average rank across all of the planetary features. Interestingly archaeological sites (cent, sip, vira, and virb) are among the top 8. This result is consistent with Arkhipov's [11], who

**TABLE 3:** *Log Likelihoods Based on Terrestrial Data. Columns are Individual log Likelihood Scores. Total is the Sum (Assuming Measurements are Uncorrelated). Negative Scores Indicate Natural; Positive Scores Artificial.*

| Image | Class | Log Likelihoods | | | | |
|---|---|---|---|---|---|---|
| | | Fractal Dimension | Fractal Model Fit | Anisotropy | Rectilinearity | Total |
| city | 1 | -0.01892015 | 0.81211409 | -0.1553787 | 1.35493244 | 1.99274765 |
| nasca | 1 | -0.02631655 | -0.0589842 | 11.2955733 | 0.37581094 | 11.5860835 |
| apc | 1 | 1.133116703 | 0.88928955 | -0.3218097 | 1.26096928 | 2.96156586 |
| penta | 1 | -0.12848822 | 0.98287998 | 2.01802089 | 1.39292189 | 4.26533454 |
| tank | 1 | 0.096359077 | 0.88737507 | -0.5986149 | 0.41037524 | 0.79549451 |
| dogr | 1 | -0.12707075 | -0.794412 | 0.94094316 | 0.58562774 | 0.60508818 |
| cent | 1 | -0.16217594 | 0.9435858 | -0.7687999 | 0.9287833 | 0.94139326 |
| ch | 1 | -0.06682392 | 0.34670495 | -0.7542915 | 1.24181034 | 0.76739986 |
| vira | 1 | -0.17181728 | 0.91683237 | -0.6537993 | -1.320984 | -1.2297683 |
| virb | 1 | -0.15307717 | 0.89755907 | -0.7438168 | 1.39773999 | 1.39840512 |
| sip | 1 | -0.15530512 | 0.63795165 | -0.7245857 | 1.3806368 | 1.13869761 |
| san | -1 | 0.00069883 | -14.868579 | 2.08841657 | 0.09514112 | -12.684322 |
| zcas | -1 | 0.228441478 | 0.73226831 | -0.7443021 | -0.0761709 | 0.14023676 |
| bad | -1 | -0.03866072 | 0.98327428 | -0.7689718 | -0.2551481 | -0.0795063 |
| bush | -1 | -0.17624662 | 0.9458857 | -0.7549882 | -0.1241245 | -0.1094737 |
| fr | -1 | -0.03145995 | 0.95825414 | -0.7760223 | -8.5712132 | -8.4204413 |
| drainyem | -1 | -0.16286438 | -0.1718265 | -0.766994 | -0.8549883 | -1.9566731 |
| cas | -1 | -0.08710323 | 0.85379618 | -0.7395464 | -10.729271 | -10.702124 |
| dogf | -1 | -0.18662649 | -5.985845 | -0.5541665 | 0.80344271 | -5.9231953 |
| zfr | -1 | 0.010270358 | 0.96241875 | -0.7007232 | 0.99423374 | 1.26619961 |
| iap | 0 | -0.05482149 | -15.594631 | -0.1250426 | 1.34698901 | -14.427506 |
| ukert | 0 | -0.15722727 | 0.65123319 | -0.4567455 | 1.34261582 | 1.37987625 |
| vik | 0 | -0.1827695 | 0.97320817 | 0.51388807 | -0.6914202 | 0.61290657 |
| arab | 0 | -0.18294492 | 0.69659534 | -0.2747345 | 1.12216684 | 1.36108279 |
| aria | 0 | -0.08067004 | 0.58384329 | -0.7491567 | 0.94792966 | 0.70194617 |
| eur | 0 | 0.494506347 | -31.146974 | 0.63872808 | 1.22693079 | -28.786809 |
| spid | 0 | -0.05176324 | -4.3163099 | -0.7305524 | 1.13484884 | -3.9637767 |
| mgs | 0 | -0.06248522 | -0.3938324 | -0.3905325 | -15.123159 | -15.970009 |
| fom | 0 | -0.11394547 | 0.98198385 | -0.7755337 | -0.2930999 | -0.2005952 |
| far | 0 | 0.353347324 | 0.09631752 | -0.4542954 | 1.24294927 | 1.23831871 |
| mdim | 0 | -0.13844426 | -6.5755052 | -0.7546653 | -4.7741523 | -12.242767 |
| themis | 0 | -0.17273029 | -19.022212 | -0.6957909 | 1.35696635 | -18.533767 |

**TABLE 4:** *Statistics of Natural and Artificial Features. Natural and Artificial Features Have Somewhat Different Fractal Model Fit, Anisotropy, and Rectilinearity Statistics but Similar Fractal Dimensions.*

| | | Fractal Dimension | Fractal Model Fit | Anisotropy | Rectilinearity |
|---|---|---|---|---|---|
| **Natural** | **Mean** | 2.607235 | 0.979111556 | 2.34921522 | -0.00367089 |
| | **Variance** | 0.076226135 | 0.000265981 | 0.44637336 | 0.275216693 |
| **Artificial** | **Mean** | 2.607345727 | 0.986838636 | 2.94948482 | 0.555262091 |
| | **Variance** | 0.111344537 | 0.000048986 | 1.49441847 | 0.090403516 |
| **Combined** | **Variance** | 0.08552524 | 0.00032128 | 0.86491989 | 0.27964493 |

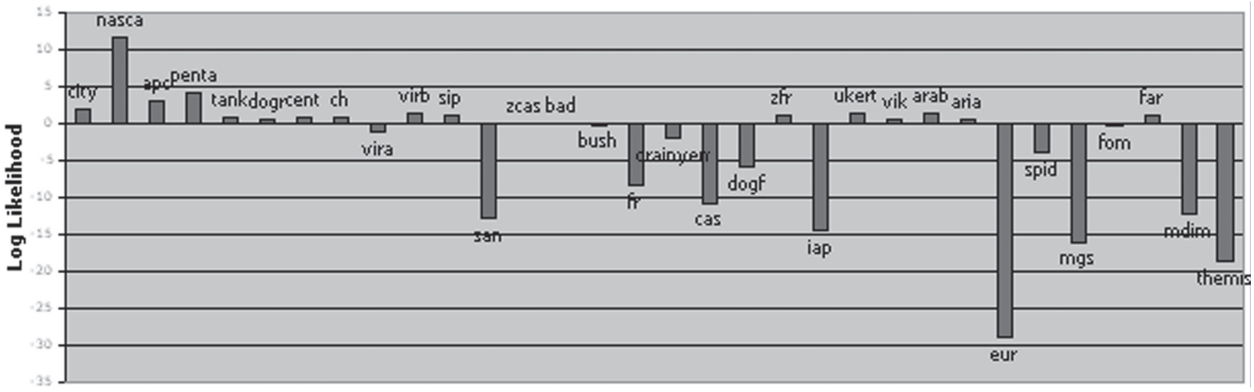


**Fig. 4 Summed log likelihoods for terrestrial and planetary images. From left to right are terrestrial images of artificial features, natural backgrounds, and images of interesting extraterrestrial features.**

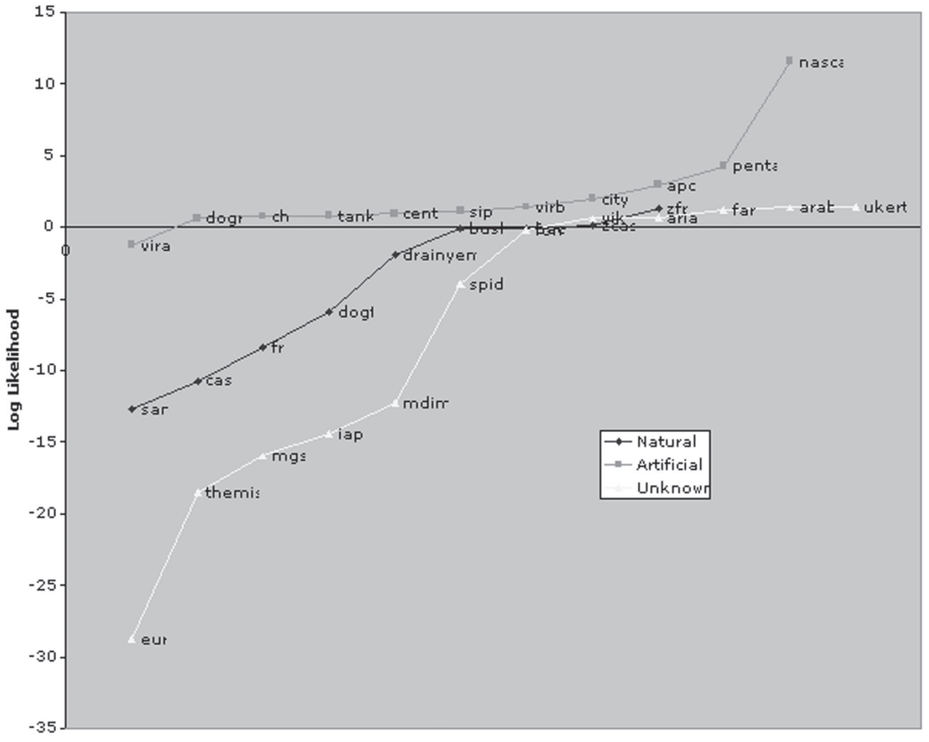


**Fig. 5 Summed log likelihoods sorted and plotted by class. Extraterrestrial features that fall above the line (positive log likelihood) are considered possibly artificial.**

developed an artificiality index and showed that a number of sites on the moon had values between that of the lunar background and terrestrial archaeological sites.

## 5. DISCUSSION

Object detection techniques seek some intrinsic property for separating objects of interest (e.g., tanks and trucks) from the background [9]. Most operate as anomaly detectors that model the natural background (noise) and detect possible objects (signals) as deviations from noise. Deviations from noise are necessary, but not sufficient, to decide that a signal is present. False alarms (neither the signals we seek nor the noise that has been modeled) occur and must be mitigated using other information. We have described an alternative approach that formulates detection as a two-class problem of deciding between signal or noise. It uses statistical models computed over a training set to characterize natural and artificial patterns empirically in terms of a set of measurements (fractal dimension, fractal model fit, anisotropy, and rectilinearity). A classification accuracy of 85% was achieved over the training set, which consisted of a variety of natural terrestrial backgrounds (fractal textures, drainage patterns, tectonic features, etc.) and artificial features (e.g., roads, cities, vehicles, archaeological ruins). The classifier was then extended and used to evaluate a collection of enigmatic lunar and planetary features. Although the data are too limited in size and scope to draw any definite conclusions, the results suggest that certain areas on our moon and on Mars appear to be artificial by comparison with terrestrial features.

Areas of future work include increasing the size and diversity of the training set, expanding and refining image measurement techniques (e.g., measuring fractal dimension over multiple scale ranges to better describe multifractal features), and exploring alternative (non-Gaussian) classification approaches.

**TABLE 5:** *Similarity Between Terrestrial and Planetary Features. Columns Correspond to Images of Planetary Features. Most Similar Features are Near the top of the Columns; Least Similar Features are at the Bottom.*

| iap | ukert | vik | arab | aria | eur | spid | mgs | fom | far | mdim | themis |
|---|---|---|---|---|---|---|---|---|---|---|---|
| dogf | virb | vira | bush | zfr | san | dogf | cas | bush | zfr | drainyem | dogf |
| san | tank | dogr | dogr | bad | dogf | sip | fr | cent | bad | fr | sip |
| dogr | cent | bush | city | virb | dogr | drainyem | vira | drainyem | virb | dogf | drainyem |
| city | zfr | tank | cent | tank | city | cent | bad | ch | zcas | cas | virb |
| drainyem | ch | drainyem | sip | zcas | drainyem | bush | drainyem | vira | tank | bush | bush |
| sip | bush | bad | ch | bush | penta | city | bush | sip | apc | vira | san |
| penta | vira | cent | drainyem | cent | sip | virb | zcas | bad | sip | dogr | dogr |
| bush | bad | zcas | dogf | sip | bush | ch | tank | virb | vira | san | zfr |
| cent | sip | penta | vira | vira | nasca | dogr | zfr | city | cent | bad | cent |
| virb | zcas | ch | virb | drainyem | cent | vira | cent | fr | bush | cent | bad |
| ch | city | dogf | penta | dogf | ch | bad | dogf | zfr | dogf | sip | city |
| vira | penta | zfr | tank | ch | virb | zfr | sip | dogr | drainyem | ch | tank |
| bad | drainyem | city | bad | city | vira | san | virb | dogf | ch | tank | vira |
| zfr | dogr | virb | zfr | apc | fr | penta | dogr | tank | city | zfr | ch |
| tank | dogf | sip | zcas | dogr | bad | tank | ch | cas | dogr | virb | zcas |
| nasca | apc | fr | san | penta | cas | fr | apc | zcas | penta | zcas | penta |
| fr | fr | cas | fr | fr | zfr | zcas | san | penta | fr | city | apc |
| zcas | san | apc | apc | cas | tank | cas | city | san | cas | penta | fr |
| cas | cas | san | cas | san | zcas | apc | penta | apc | san | apc | cas |
| apc | nasca | nasca | nasca | nasca | apc | nasca | nasca | nasca | nasca | nasca | nasca |

**TABLE 6:** *Overall Similarity Between Terrestrial and Planetary Features. Half of the More Frequent Terrestrial Analogs are Archaeological Sites (cent, sip, vira, virb, dogr).*

| | |
|---|---|
| **More Frequent (top 50%)** | bush |
| | drainyem |
| | cent |
| | dogf |
| | sip |
| | vira |
| | virb |
| | bad |
| | dogr |
| | zfr |
| **Less Frequent (bottom 50%)** | ch |
| | tank |
| | city |
| | zcas |
| | san |
| | penta |
| | fr |
| | cas |
| | apc |
| | nasca |

## REFERENCES


1. G. Cocconi and P. Morrison, "Searching for interstellar communications," in *Interstellar Communication*, A.G.W. Cameron (ed), W. A. Benjamin, New York, 1963.
2. The Search for Extraterrestrial Intelligence (SETI) in the Optical Spectrum, *SPIE Proceedings of the First International Conference on Optical SETI*, **1867**, Los Angeles CA.
3. G.V. Foster, "Non-human artifacts in the solar system", *Spaceflight*, **14**, pp.447-453, 1972.
4. R.A. Freitas, "The Search for Extraterrestrial Artifacts (SETA)", *JBIS*, **36**, pp.501-506, 1983.
5. C. Sagan, "The recognition of extraterrestrial intelligence", *Proceedings of the Royal Society*, **189**, pp.143-153, 1975.
6. L. Leopold and W. Langbein, The concept of entropy in landscape evolution", *USGS Professional Paper 500A*, 1962.
7. R.E. Horton, "Erosional development of streams and their drainage basins; hydrophysical approach to quantitative morphology", *Bull. Geol . Soc. Am.*, **56**, pp.275–370, 1945.
8. D.M. Mark and P.B. Aronson, "Scale-dependent fractal dimensions of

topographic surfaces: An empirical investigation, with applications in geomorphology and computer mapping", *Mathematical Geology*, **16**, pp.671-683, 1984.
9. M.C. Stein, "Fractal image models and object detection", *Society of Photo-optical Instrumentation Engineers,* **845**, pp.293-300, 1987.
10. M.J. Carlotto and M.C. Stein, "A method for searching for artificial objects on planetary surfaces", *JBIS*, **43**, pp.209-216, 1990.
11. Alexey V. Arkhipov, "Towards Lunar Archaeology", *New Frontiers in Science*, **1**, pp.1-22, 2002.
12. Mark Carlotto, "Enigmatic Landforms in Cydonia: Geospatial Anisotropies, Bilateral Symmetries, and Their Correlations", *Sixth International Conference on Mars*, Pasadena, CA, July 20-25, 2003.
13. B.B. Mandelbrot, *The Fractal Geometry of Nature*, W.H. Freeman, New York, 1983.
14. R.F. Voss, "Fractals in nature: from characterization to simulation", in *The Science of Fractal Images*, H-O Peitgen and D. Saupe (ed), Springer-Verlag, New York, 1988.
15. Marilyn Bridges, *Planet Peru, An Aerial Journey through a Timeless Land*, Kodak/Aperture Books, 1991.
16. Peter K. Ness and Greg M. Orme, "Spider Ravine Models and Plant Like Features on Mars - Possible Geophysical and Biogeophysical Modes of Origins", *JBIS*, 55, pp.85-108, 2002.

*(Received 8 September 2006)*

* * *